Physica B 597 (2020) 412387

Contents lists available at ScienceDirect

Physica B: Physics of Condensed Matter

journal homepage: http://www.elsevier.com/locate/physb

Effect of Sb substitution on structural, morphological and electrical properties of $BaSnO_3$ for thermoelectric application

Palani Rajasekaran [a], Yuki Kumaki [b], Mukannan Arivanandhan [c], Mohamed Mathar Sahib Ibrahim Khaleeullah [a], R. Jayavel [c], Hiroshi Nakatsugawa [d], Yasuhiro Hayakawa [a], Masaru Shimomura [a,b,*]

[a] Graduate School of Science and Technology, Shizuoka University, Hamamatsu, 432-8011, Japan
[b] Graduate School of Integrated Science and Technology, Shizuoka University, Hamamatsu, 432-8561, Japan
[c] Centre for Nanoscience and Technology, Anna University, Chennai, 600025, India
[d] Graduate School of Engineering, Yokohama National University, Yokohama, 240-8501, Japan

ARTICLE INFO

Keywords:
Polymerization complex method
Seebeck coefficient
Structural defects
Figure of merit
Perovskite metal oxide
Band structure

ABSTRACT

Sb-substituted $BaSnO_3$ (BSO) perovskite microstructures were synthesized by a polymerization complex method with Sb concentrations of 0, 1, 5, and 10 mM. The electronic band structures of pure BSO and Sb-substituted BSO were theoretically verified by density functional theory. The findings indicated that the conduction band property was primarily attributed to the Sb-5s and Sn-5s orbitals. The Sb^{5+} donor and the subsequent oxygen vacancy enhanced electronic conduction. A high Seebeck coefficient of 58.9 μV/K and power factor of 2.1 $\mu Wm^{-1}K^{-2}$ were achieved for the 10 mM Sb-substituted BSO at 820 K. The semiconductor to metallic transition was observed at 700 K owing to the charge compensation between Sb^{5+} and Sn^{4+} ions. The structural defects and grain boundaries contributed to a low thermal conductivity in the samples. The 10 mM Sb-substituted BSO sample exhibit the dimensionless figure of merit of 0.28×10^{-2} at 820 K.

1. Introduction

The electrical energy consumption of electronic gadgets, household appliances, and vehicles has been increasing day by day. However, the energy generated by thermal power plants, nuclear power plants, and hydropower plants is not enough to requirements. About 66% of energy is wasted by vehicles, incinerators, industries, and thermal power plants. An alternative is required to supplement the power generation [1]. Thermoelectrics (TE) is promising to generate electricity from waste heat. TE technology has several advantages as it is nontoxic, scalable with low cost, highly reliable, durable, compact, and silent.

The performance of a thermoelectric material is evaluated by dimensionless figure of merit (ZT) = $S^2\sigma T\kappa^{-1}$, which is defined by Seebeck coefficient (S), electrical conductivity (σ), operating temperature (T), and thermal conductivity (κ). Thermal conductivity is composed of electronic thermal conductivity (κ_e) and lattice thermal conductivity (κ_{ph}). To increase ZT, S and σ are increased and κ is decreased. Thermal conductivity can be decreased by nano-structuring and defect engineering without affecting the electronic transport properties, thereby enhancing ZT [2–4].

Sb_2Te_3, PbTe, and Bi_2Te_3 materials have been developed for low and intermediate temperature-range thermoelectric applications. These materials cannot be used for high-temperature applications because they are easily oxidized in air. Therefore, new earth-abundant materials with low cost are required for high-temperature applications [5–7].

Metal oxide-based materials have been utilized for high-temperature TE applications because of advantages such as high thermal stability, nontoxicity, and low cost. Several *p*-type metal oxide-based materials have been reported, such as $Na_2Co_2O_4$ and $Ca_3Co_4O_9$ [8]. However, the literature on *n*-type oxide TE materials is still limited. Perovskite-based metal oxide materials have been ideal candidates for TE applications since they are highly stable in air [9,10]. The perovskite structure can be represented by ABO_3, where, A is the alkaline earth metal and B is the transition metal. $BaSnO_3$ (BSO) is one of the most promising perovskite materials with a wide band gap of 3.1 eV. The BSO has a primitive cubic structure with Sn-O-Sn bond in SnO_6 octahedral network. It has Sn^{4+}-occupied 6-fold co-ordination of oxygen atoms with Ba^{2+} as the center atoms. The valence-band maximum comprises the O 2p band and

* Corresponding author. Graduate School of Science and Technology, Shizuoka University, 3-5-1 Johoku, Naka-ku, Hamamatsu, 432-8011, Japan.
E-mail address: shimomura.masaru@shizuoka.ac.jp (M. Shimomura).

https://doi.org/10.1016/j.physb.2020.412387
Received 22 January 2020; Received in revised form 18 May 2020; Accepted 15 July 2020
Available online 28 July 2020

conduction-band minimum comprises the Sn 5s antibonding orbitals. The electronic structure of BSO can be modified by substituting hetero-valence elements such as La or Sb in the Ba or Sn sites [11–15].

Shin et al. [16] synthesized BSO for the perovskite solar cell, which is replaced by TiO_2 nanoparticles in the n-transport layer. La-doped BSO single crystal with a mobility of 300 cm^2/V-s and good optical transparency was grown by Cu_2O flux method as demonstrated by Kim et al. [17]. Cava et al. [18] grew Sb-doped BSO and achieved electrical conduction ten times larger than that of BSO. Mizoguchi et al. [19] synthesized Sb-doped BSO by solid-state reaction method and achieved electrical conductivity of 4 S/cm by addition of Sb to the Sn site. The thermoelectric properties of La-doped BSO were analyzed and the ZT value of 0.11 at 1073 K was obtained by Yasukawa et al. [20]. However, a comprehensive study of the electronic structure and thermoelectric properties of Sb-substituted BSO has not been done.

In the present study, pure BSO and Sb-substituted BSO perovskite materials were synthesized using the polymerization complex method. The initial Sb concentration in the sample was varied through 1, 5, and 10 mM. The electronic band structure was calculated using density functional theory (DFT). The structural, morphological, electrical, and thermoelectric properties such as Seebeck coefficient, electrical conductivity, and thermal conductivity were measured experimentally and the effect of Sb was discussed.

2. Experimental and theoretical procedures

The precursor materials $Ba(NO_3)_2$, $SbCl_3$, $SnCl_2{\cdot}2H_2O$, ethylene glycol (EG), ethanol, and citric acid (CA) were purchased from Wako pure chemicals and used without further purification. To synthesize BSO, the ratio of $Ba(NO_3)_2$ and $SnCl_2{\cdot}2H_2O$ was fixed as stoichiometric molar ratio of 100 mM:100 mM. They were initially dissolved in 100 mL of EG solution and stirred vigorously under 353 K for 1 h. 100 mL of CA (100 mM) solution prepared with ethanol was then added. The reaction was continued at 408 K for 24–28 h to promote the polymerization reaction. A brown-color solution was obtained after the completion of the reaction. The gel solution was annealed at 623 K for 3 h in air to remove the excess solvents from the gel solution. After the completion of annealing, a black-colored powder was obtained. The powder was again annealed at 1123 K for 5 h and at 1173 K for 24 h. Finally, the powder color was changed to white. The collected powder was fired at 1473 K for 10 h under open atmosphere. A similar procedure was followed to synthesize Sb-substituted BSO. To prepare Sb substituted BSO, $SbCl_3$ was added into the precursor solution at the molar concentrations of 1, 5, and 10 mM. The disc-shaped pellets were prepared by a high-pressure and high-temperature sintering process for electrical and thermal transport characterizations. The structural patterns of the samples were analyzed by X-Ray diffraction (XRD) using Rigaku Ultima III. The wavelength of Cu Kα was 1.54 Å with scan rate of 0.02 deg/min and diffraction patterns were recorded between 20° to 70°. The surface morphology of the microstructure was analyzed using analytical field-emission scanning electron microscopy (FE-SEM, JEOL-7001F). Grain size distribution of the samples was analyzed using ImageJ software [21,22]. The elemental average values were measured by JXA-8530F field emission electron probe microanalysis (EPMA). The morphological structure was measured by scanning transmission electron microscopy with energy dispersive X-ray spectroscopy (STEM-EDX) using JEOL-2001F with an accelerating voltage of 200 kV. The enlarged crystallographic structural morphology was measured by high-resolution transmission electron microscopy (HRTEM).

The chemical states of each element were analyzed by X-ray photoelectron spectroscopy (XPS) with the monochromatic Al Kα (1486.6 eV) source (AXIS ULTRA, Kratos). Binding energy calibration was achieved by the carbon peak at 285.0 eV. The thermoelectric properties of S and σ were measured as a function of temperature from 300 to 820 K using a self-made system [23]. The thermal diffusivity (α) was measured using cylindrical pellets with 10 mm diameter and 1 mm height under a nitrogen atmosphere by the laser flash method (model TC-7000, ULVAC-RIKO). The specific heat capacity (C_p) was measured by differential scanning calorimetry (DSC) (DSC 60 Plus, Shimadzu) under an argon atmosphere and the sample density (D) was measured using the Archimedes method. The measured density values were found by 5.125 g/cm^3 and 5.09 g/cm^3 for Sb: 5 mM and Sb: 10 mM. The thermal conductivity was calculated using the formula:

$$\kappa = \alpha C_p D \quad (1)$$

The electronic band structures of the pure and Sb-substituted BSO model were calculated by Quantum ESPRESSO based on DFT [24] using a 3 × 3 × 3 supercell [25,26]. For the Sb-substituted system, a single Sn atom located at the center of the supercell was substituted by the Sb atom. The projector-augmented-wave (PAW) method was employed with the Perdew-Burke-Ernzerhof (PBE) functional as the exchange and correlation potential for the generalized gradient approximation (GGA). For the structural optimization calculation, the Broyden–-Fletcher–Goldfarb–Shanno (BFGS) quasi-newton algorithm was used until the total forces reached less than 1.0×10^{-5} Ry $Bohr^{-1}$. Subsequently, k-space integration was performed using a 6 × 6 × 6 mesh within the Monkhorst-Pack k-point sampling. The kinetic-energy cutoff of wave functions and charge density were 47 Ry and 187 Ry, respectively.

3. Results and discussion

3.1. Electronic band structures of pure and Sb-substituted BSO

The band structure of Sb-substituted BSO is shown in Fig. 1(a). As shown in Fig. 1(a), the Fermi level of Sb-substituted BSO was located within the lowest empty band whereas, the position of the pure BSO was within the gap [27]. This implies that carrier concentration increased by Sb doping. For further analysis of the electronic states near the Fermi level, the projected density of states (PDOS) of the Sb-substituted BSO were calculated and shown in Fig. 1 (b & c). The results revealed that the density of states near the conduction band edge composed of Sb 5s and Sn 5s orbitals which mainly contributed for electronic conduction in the conduction band as shown in Fig. 1(b). This led to the conclusion that the first Sn 5s orbital interacts with O 2p orbitals. The BSO band consists of Sn 5s- O 2p σ* orbital interactions in pure case [27]. Therefore, the metal-oxygen bonding, Sb 5s-O 2p σ* orbital, is considered for the conduction mechanism of Sb-substituted BSO. Thus, the doping of Sb onto the Sn site modifies the Fermi-level position from insulating to semiconductor property. Further, PDOS of the first-, second- and third-nearest-Sn atoms from the Sb atom (the distances from the Sb atom are 4.116, 5.820, and 7.129 Å, respectively) have been analyzed and are shown in Fig. 1(c). It concluded that PDOS of Sn 5s for the first nearest atom is larger compared to those of the second and third nearest Sn atoms at Fermi level. It is also the local electronic structural effect of the Sb doping. The Ba 6s, Ba 5s, and O 2s orbitals are not the majority states of the conduction band edge.

3.2. Microstructural analysis and elemental analysis

Fig. 2 shows the X-ray diffraction (XRD) patterns of pure BSO and Sb-substituted BSO. The high-intensity diffraction peaks appeared at 30.72°, 37.02°, 44.02°, 54.61°, and 63.94° which were indexed as (110), (111), (200), (211), and (220) planes, respectively. These diffraction peaks were in good agreement with the JCPDS no 15-0780 for pure BSO-cubic perovskite structure $Pm\bar{3}m$. There was no shift in the diffraction peaks of the XRD patterns of the Sb-substituted BSO sample, which indicates that a small amount of Sb did not affect the perovskite crystal structure.

The stability of the geometric distortion of perovskite structure is estimated by the tolerance factor $t = \frac{R_A + R_O}{\sqrt{2}(R_B + R_O)}$, where R_A, R_B, and R_O are

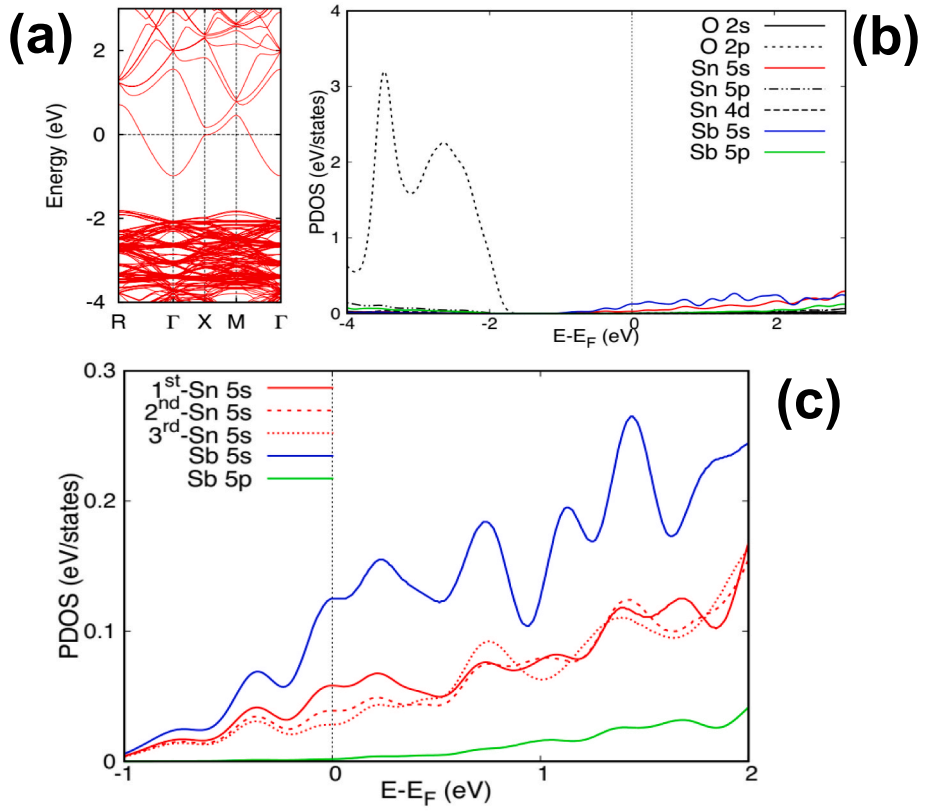

Fig. 1. (a) Calculated Sb-substituted BSO band structure. (b) PDOS of the Sb-substituted BSO with wide-range. (c) PDOS near the Fermi level.

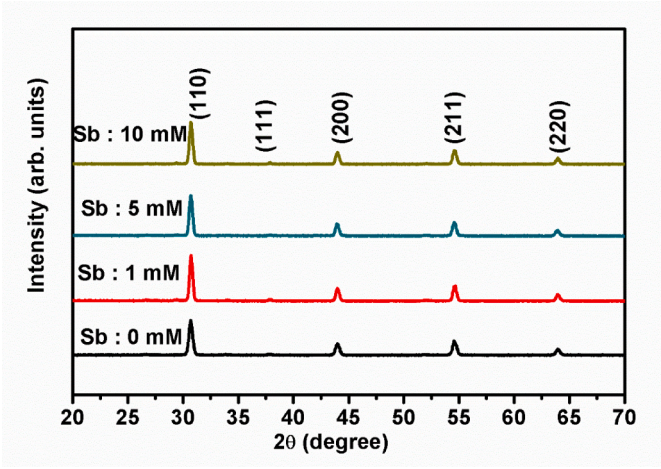

Fig. 2. X-ray diffraction (XRD) patterns of pure and Sb-substituted BSO samples. (Sb: 0, 1, 5, and 10 mM) sintered at 1473 K for 10 h.

the ionic radii of Ba (0.135 nm), Sn (0.069 nm), and O (0.138 nm) ions, respectively [28]. The tolerance factor of pure BSO was calculated to be 1.026, which indicated the cubic structure. The lattice constant was extracted from the high-intensity diffraction peak of (110) plane and estimated as 4.117 Å, 4.114 Å, 4.119 Å, and 4.117 Å for the Sb content of 0, 1, 5, and 10 mM, respectively. The lattice parameters were nearly same for all the samples.

The morphologies and size distributions of the pure and Sb-substituted BSO samples are shown in Fig. 3 with corresponding histograms. Fig. 3(a) shows the SEM image of pure BSO image, which confirmed the cubic morphology. The cubic morphology was retained for the Sb-substituted BSO as shown in Fig. 3(b–c). The average particle size, which is estimated by the distribution curve, varied as 0.64, 0.50, and 0.80 μm for pure BSO, 5 mM Sb-substituted BSO, and 10 mM Sb-substituted BSO, respectively. The average particle size is not significantly affected after Sb substitution.

Fig. 4(a–b) show HRTEM images of the 5 mM Sb-substituted BSO. The inset in Fig. 4 (a) shows a fast Fourier transform (FFT) pattern, which confirmed the single phase. The lattice fringes with the d-spacing of 0.3 nm was observed in Fig. 4(b) which agrees with the (110) plane of BSO. The HRTEM images of 10 mM Sb-substituted BSO are shown in Fig. 4(c–d). The distance of lattice fringes was 0.29 nm, which also indicated the (110) plane. Stack layers and grain boundaries were also observed, as indicated by the dotted circles in Fig. 4(b–d), which implies rigid interparticle connections.

The chemical states were characterized by XPS. Fig. 5 (a) and (b) show the Sn 3d and O 1s spectra of pure BSO, respectively. The Sn 3d core-level spectrum is fitted with Sn $3d_{3/2}$ and Sn $3d_{5/2}$ components at 497 eV and 488.5 eV with spin-orbit splitting energy of 8.5 eV. Fig. 5 (c) and (d) show the respective Sn 3d and Sb 3d spectra of Sb-substituted BSO (Sb: 5 mM), and Fig. 5 (e) and (f) show the spectra of Sb-substituted BSO (Sb: 10 mM). The Sn $3d_{5/2}$ binding energies shifted to 486.9 eV for the 5 mM Sb-substituted BSO and 10 mM Sb-substituted BSO samples. This is attributed to the shift of the Fermi-level position by doping of Sb in the Sn site as indicated by our DFT calculation.

The oxygen O 1s core-level spectrum is deconvoluted into three components: lattice oxygen (LO), vacancy-related oxygen, where an adsorbed oxygen molecule reacts with oxygen vacancy at the subsurface (VO) [29,30], and surface hydroxyl group (O-H) as shown in Fig. 5(b, d, f). The O 1s binding energies of the pure sample for LO, VO, and O-H were 531.8, 533.3, and 534.4 eV, respectively. The calculated VO/LO ratios for pure BSO, Sb-substituted BSO (Sb: 5 mM), and Sb-substituted BSO (Sb: 10 mM) were 0.79, 0.43, and 0.94, respectively. The VO/LO ratio was found to be low for the sample with the Sb concentration of 5 mM. However, the VO/LO ratio was observed to increase by increasing

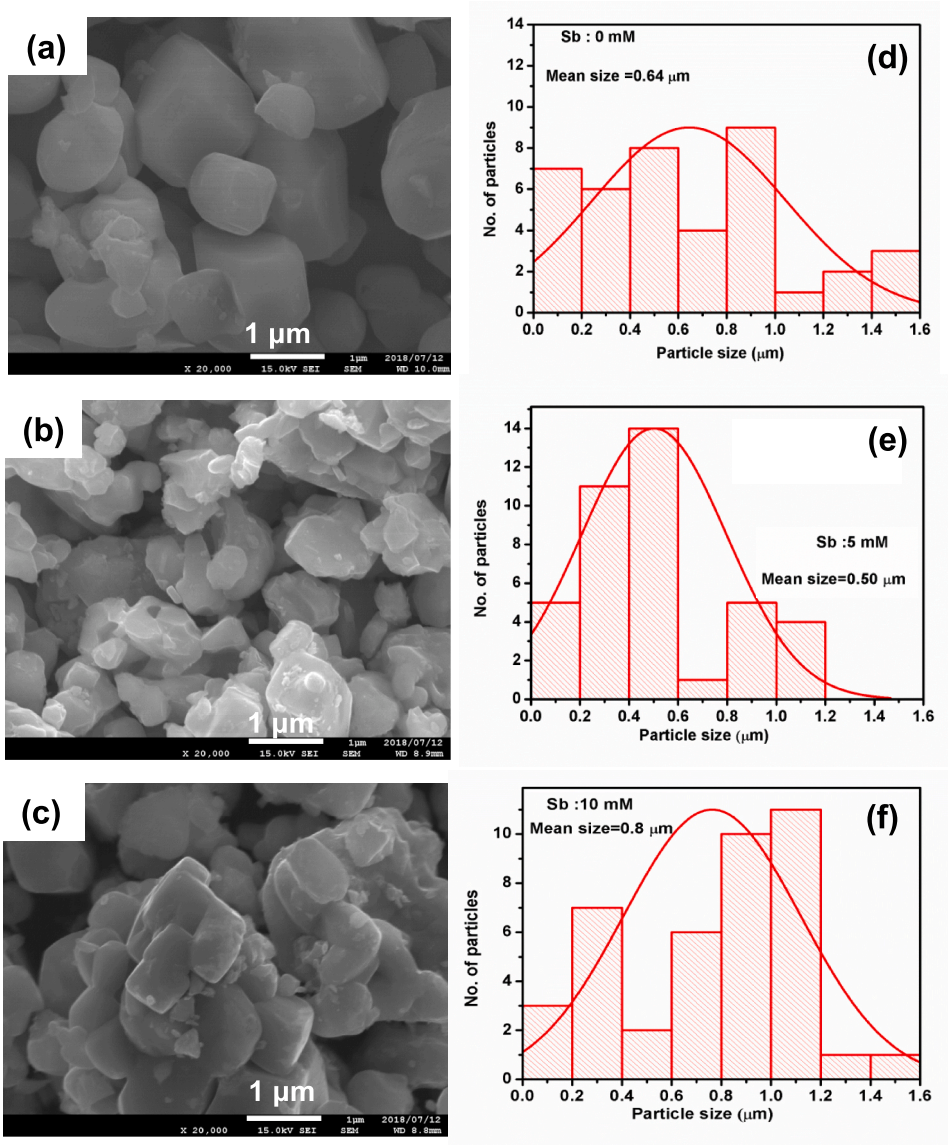

Fig. 3. (a–c) SEM images and (d–f) size distributions of BSO samples. (a, d) 0 mM, (b, e) 5 mM, and (c, f) 10 mM of Sb-substituted BSO.

the Sb concentration to 10 mM. The lowest VO/LO ratio for the sample with an Sb concentration of 5 mM can be attributed to the minimum averaged size observed in the field emission scanning electron microscopy (FESEM) image as shown in Fig. 3(b) with a low density of the oxygen vacancy.

The intensity of Sb $3d_{5/2}$ core-level binding energy peak increased by increasing the Sb concentration. The Sb $3d_{5/2}$ (Sb^{5+}) binding energies of Sb-substituted BSO (Sb: 5 mM) and Sb-substituted BSO (Sb: 10 mM) were found to be 531.4 and 531.5 eV, respectively. No trivalent state of Sb^{3+} was identified. In the case of the Sb^{5+} ions substituted on the Sn^{4+} site, Sb acted as the donor providing free electrons to the conduction band which is consistent with recently reported thin film based Sb-doped BSO [31]. The calculated Sb to Sn ratio by XPS values were 0, 0.056, and 0.073 for pure BSO, Sb-substituted BSO (Sb: 5 mM), and Sb-substituted BSO (Sb: 10 mM), respectively. The element verification by element probe micro analysis ratio values were 0, 0.053, and 0.082 for pure BSO, Sb-substituted BSO (Sb: 5 mM), and Sb-substituted BSO (Sb: 10 mM), respectively as shown in Table 1. The surface sensitivity of both measurements was different, but the antimony to tin ratio was almost identical, confirming that all elements were uniformly distributed in the structure. The generation of free charge carriers originated from the Sb^{5+} substitution on the Sn site by donating the excess electrons to the conduction band, thereby forming an oxygen vacancy and subsequently, the electrical conductivity increased as shown by the XPS spectra of Sb 3d and O 1s [32].

3.3. Thermoelectric properties

The electrical resistivity, carrier concentration, and mobility of Sb-substituted BSO measured at room temperature are summarized in Table 2. The negative sign of Hall coefficient confirmed the *n*-type semiconductors. The electrical resistivity decreased by increasing Sb content and a minimum value of 0.07 (Ω-cm) at Sb: 10 mM was achieved. The carrier concentrations increased from 1.08×10^{19} to 3.03×10^{19} cm^{-3} by increasing Sb content from 1 to 10 mM. These enhancements are due to the substitution of Sb on the Sn site of BSO. The substitution of Sb^{5+} on the Sn^{4+} site generates more electrons, thereby increasing the carrier concentration. The carrier mobility decreased with the increase in Sb content in the sample due to high carrier concentration.

The S values of Sb-substituted BSO (Sb: 5 mM) and Sb-substituted BSO (Sb: 10 mM) were measured from 300 to 820 K as shown in Fig. 6. The negative values indicate the presence of *n*-type semiconductor. Since pure BSO was used as the insulator, the S value could

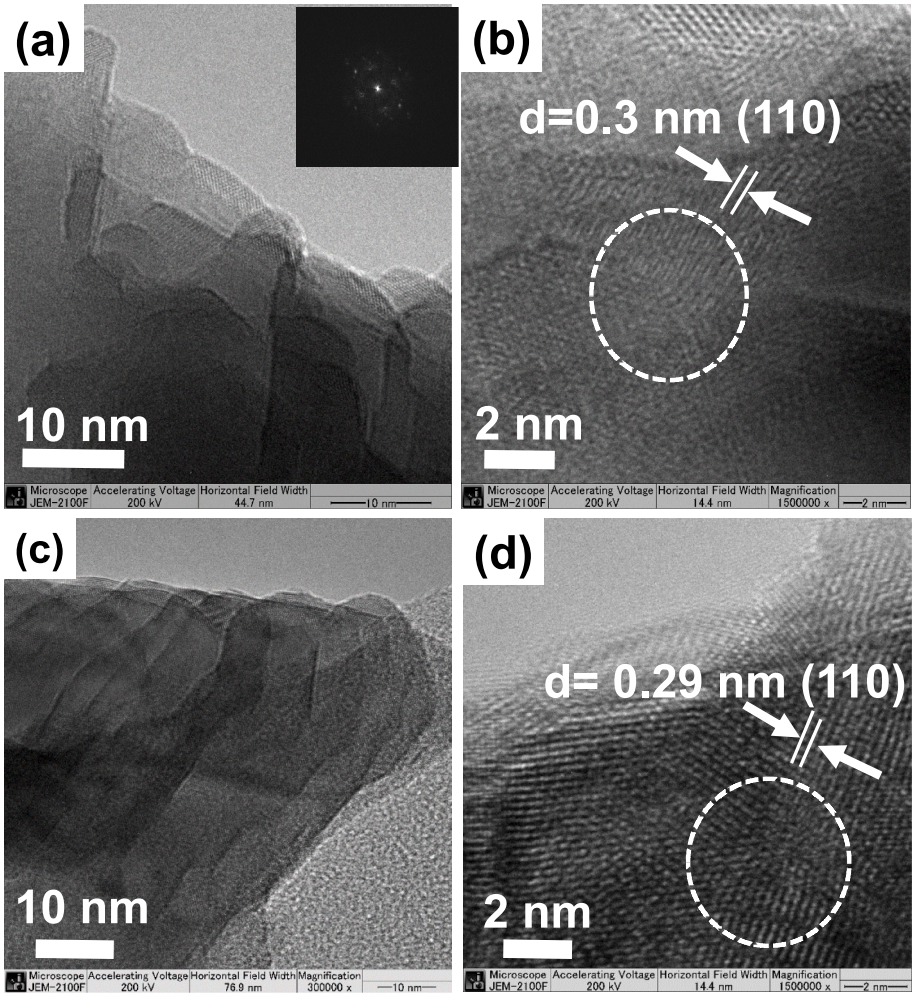

Fig. 4. HRTEM images of (a, b) Sb-substituted (Sb: 5 mM) and (c, d) Sb-substituted BSO (Sb: 10 mM) samples.

not be measured. The measured S values are monotonically increased with the increase in temperature. The S values were similar for the Sb-substituted BSO (Sb: 5 mM) and Sb-substituted BSO (Sb: 10 mM) up to 800 K. When the temperature increased beyond 800 K, a slight change in the S values was observed. The difference was 2.44 μV/K. The S value of Sb-substituted BSO (Sb: 10 mM) was 58.9 μV/K at 820 K, which was higher than that of Sb-substituted BSO (Sb: 5 mM) 56.4 μV/K at the same temperature.

The σ value of Sb-substituted BSO was measured as a function of temperature using four-probe method from 300 to 820 K as shown in Fig. 7 (a). The σ value was found to be low at room temperature, but it significantly increased with an increase in temperature as the localized electrons were thermally excited. Moreover, the electrical conductivity of both the samples increased with temperature which shows the semiconducting behavior of the samples. The high σ value of 630 S/m at 820 K was achieved for the 10 mM Sb-substituted BSO, which was higher than that of 5 mM Sb-substituted BSO (270 S/m) at the same temperature. The σ value increased with the increase in Sb concentration which confirms that the incorporation of heterovalent Sb increases the carrier density in the BSO as shown in Table 2. According to DFT, the Sb 5s is one of the main orbitals which determine the Fermi level. Subsequently, even a small amount of Sb ions can directly increase the σ value. Semiconductor-to-metallic transition was observed for the Sb-substituted BSO (Sb: 5 mM) at a high temperature. This is shown by the charge compensation between the Sn^{4+} and Sn^{2+} ions.

The Arrhenius plot of log σ versus 1000/T (K^{-1}) is shown in Fig. 7(b) and the equation is given by:

$$\sigma = A \exp\left(-\frac{E_a}{k_B T}\right) \quad (2)$$

where A is the pre-exponential constant, E_a: activation energy, k_B: Boltzmann constant, T: absolute temperature. The calculated activation energy (E_a) for the Sb-substituted BSO (Sb: 5 mM) and Sb-substituted BSO (Sb: 10 mM) was 0.014 eV and 0.013 eV, respectively, at the semiconducting region. This indicated that the impurity scattering was dominant in this region. A similar behavior was observed as previously reported [33,34].

The thermoelectric power factor ($S^2\sigma$) was calculated using the measured S and σ values and the variation of power factor as a function of temperature is shown in Fig. 8. The power factor of both samples increased with temperatures. The power factor of 10 mM Sb-substituted BSO was 2.1 $\mu Wm^{-1}K^{-2}$ at 820 K which is relatively higher than that of 5 mM Sb-substituted BSO (0.8 $\mu Wm^{-1}K^{-2}$) at the same temperature. The high power factor of 10 mM Sb-substituted BSO was originated from the high electrical conductivity and reasonable Seebeck coefficient.

The κ value was measured as a function of temperature as shown in Fig. 9 and was found to decrease with the increase in temperature from 300 to 900 K for both samples. The κ value of Sb-substituted BSO (Sb: 10 mM) was smaller than that of (Sb: 5 mM). However, the difference was negligible. The total thermal conductivity ($\kappa = \kappa_e + \kappa_{ph}$) is composed of electronic thermal conductivity (κ_e) and lattice thermal conductivity (κ_{ph}). The κ value at room temperature was approximately 1.04 and 0.94 W/mK at 300 K for the Sb-substituted BSO (Sb: 5 mM) and the Sb-substituted BSO (Sb: 10 mM), respectively.

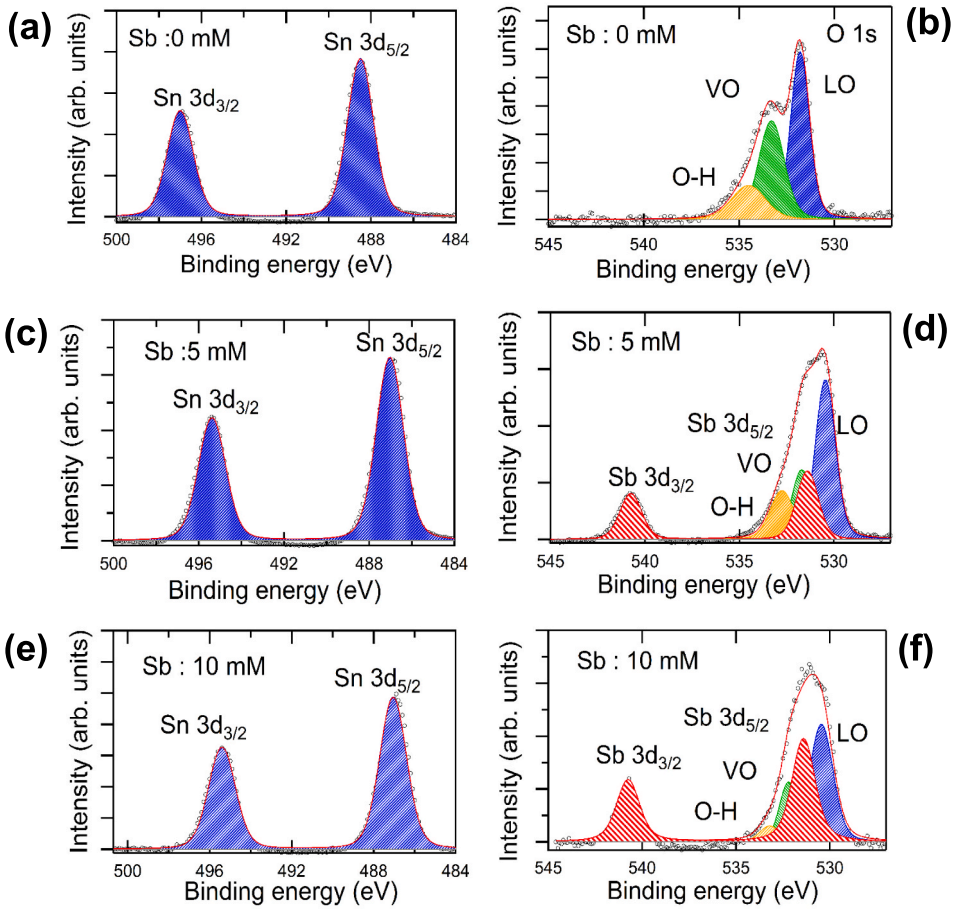

Fig. 5. Core-level spectra of (a, b) pure BSO, (c, d) Sb-substituted BSO (Sb: 5 mM), and (e, f) Sb-substituted BSO (Sb: 10 mM). (a, c, e) Sn 3d and (b, d, f) O 1s with Sb 3d spectra.

Table 1
Sb to Sn elemental ratio of XPS, EPMA, and experimental values.

Sample name	XPS (Sb/Sn)	EPMA (Sb/Sn)	Experimental source (Sb/Sn)
Sb: 0 mM	0.000	0.000	0.000
Sb: 5 mM	0.056	0.053	0.050
Sb: 10 mM	0.073	0.082	0.100

Table 2
Hall measurements of Sb-substituted BSO.

Sample	Electrical resistivity (Ω-cm)	Carrier concentration (× 10^{19} cm^{-3})	Mobility (cm^2/V-s)
BSO (Sb: 1 mM)	0.51	1.08	1.14
BSO (Sb: 5 mM)	0.47	2.35	0.57
BSO (Sb: 10 mM)	0.07	3.03	0.26

The κ_e value was calculated using the following equation:

$$\kappa_e = L\sigma T \quad (3)$$

where L is the Lorentz number (2.44×10^{-8} V^2K^{-2}), σ is the electrical conductivity, and T is the absolute temperature. The lattice thermal conductivity was derived from the measured total κ and calculated κ_e. Table 3 shows the calculated Cp, κ_{ph} and κ_e values of Sb-substituted BSO. The electronic thermal conductivity increased as the temperature

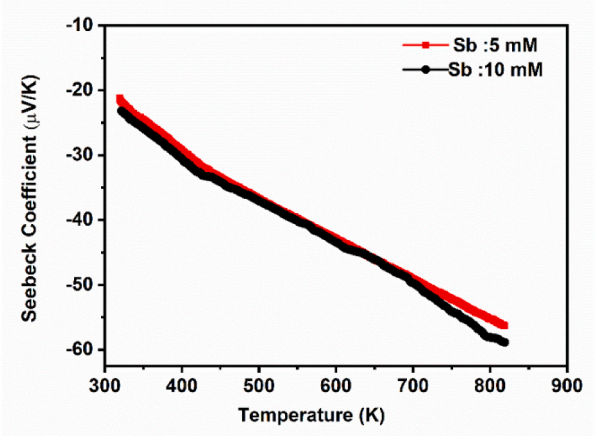

Fig. 6. The S value of Sb-substituted BSO (Sb: 5 mM) and Sb-substituted BSO (Sb: 10 mM).

increased. However, the κ_e contribution was very small, implying that the κ_{ph} contribution was dominant.

The κ value decreased with the increase in temperature due to the phonon–phonon scattering at the microstructure. The κ value also decreased as the Sb concentration increased [35]. This can be attributed to the following reasons: (i) The VO/LO ratio, which was increased by the addition of the Sb ions, generated additional phonon scattering (ii) The nanostructured grain boundary at the interfaces significantly

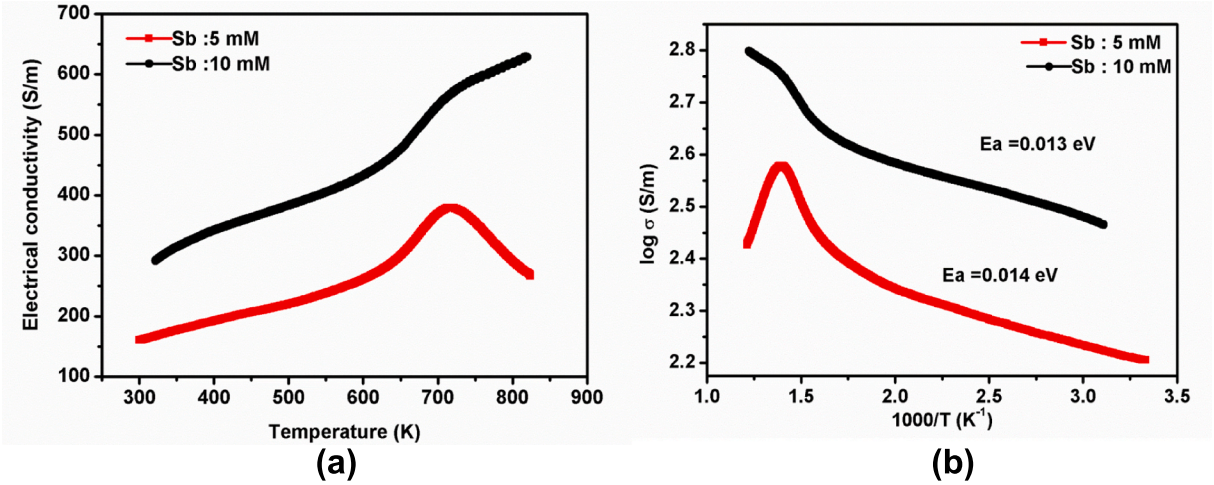

Fig. 7. (a) Electrical conductivity of 5 mM and 10 mM Sb-substituted BSO samples, (b) Arrhenius plot of log σ Vs 1000/T (K^{-1}).

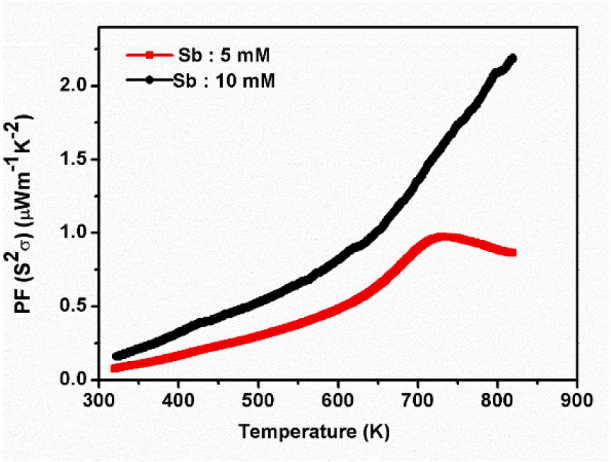

Fig. 8. The $S^2\sigma$ value of Sb-substituted BSO (Sb: 5 mM) and Sb-substituted BSO (Sb: 10 mM).

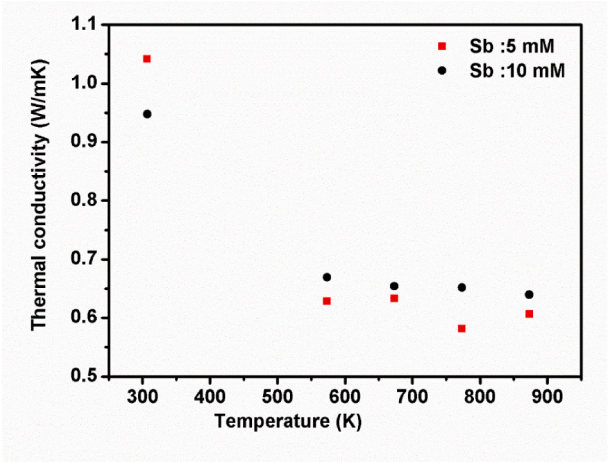

Fig. 9. Temperature dependence of the total thermal conductivity of (a) Sb-substituted BSO (Sb: 5 mM) and Sb-substituted BSO (Sb: 10 mM).

affected the phonon mean free path as shown by the scanning electron microscopy (SEM) and HRTEM images. These structural defects and grain boundary contributed to low thermal conductivity. (iii) The

Table 3
Calculated κ_{ph}, κ_e and Cp values of Sb-substituted BSO (Sb: 5 mM and 10 mM).

Temperature (K)	(Sb: 5 mM)			(Sb: 10 mM)		
	(κ_{ph}) W/mK	(κ_e) mW/mK	Cp (J/gK)	(κ_{ph}) W/mK	(κ_e) mW/mK	Cp (J/gK)
321	1.04	1.30	0.371	0.94	2.29	0.283
573	0.62	3.48	0.363	0.66	5.85	0.314
673	0.62	5.47	0.392	0.64	8.39	0.322
773	0.57	6.11	0.379	0.64	11.4	0.330
820	0.59	5.45	0.393	0.62	12.6	0.326

reduction of average grain size from 0.5 to 0.8 μm for the Sb-substituted BSO ((Sb: 5 mM) and (Sb: 10 mM)) introduced significant scattering of phonons, thus reducing the κ value.

The thermoelectric figure of merit is calculated using the Seebeck coefficient (S), electrical conductivity (σ) and thermal conductivity (κ) values of 5 mM and 10 mM Sb-substituted BSO, as shown in Fig. 10. The ZT of 10 mM Sb-substituted BSO is relatively higher than that of 5 mM Sb substituted sample at all measured range of temperatures. For instance, 10 mM Sb-substituted BSO exhibited ZT of 0.28×10^{-2} at 820 K which is relatively higher than that of 5 mM Sb substituted sample (0.11×10^{-2}) at the same temperature. The substitution of Sb^{5+} ions on the Sn site increased carrier concentration thereby electrical

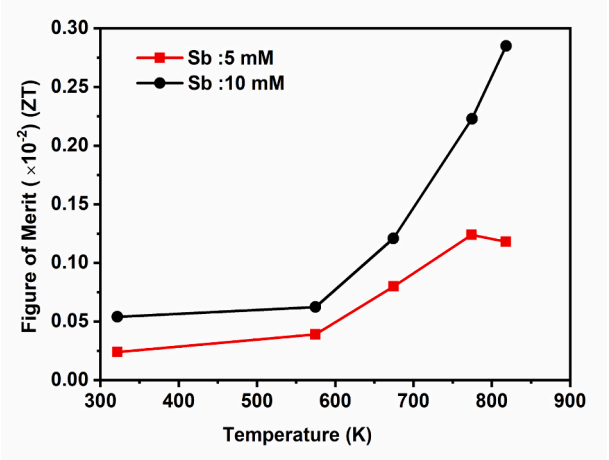

Fig. 10. Dimensionless figure of merit (ZT) of 5 mM Sb-substituted and 10 mM Sb -substituted BSO samples.

conductivity which resulted high ZT of 10 mM Sb-substituted BSO sample. The obtained ZT is comparable with the tin oxide (SnO) based material achieved ZT (0.2×10^{-2}) at 525 K [35]. To the best of our knowledge this is the first report on Sb-doped BSO perovskite materials of electronic structure and thermoelectric properties discussed. Further investigation is required for enhancement of ZT.

4. Conclusion

Sb-substituted BSO perovskite microstructures were synthesized using the polymerization complex method. The doping concentrations of Sb were varied as 0, 1, 5, and 10 mM. The crystal structural and surface morphological investigation showed a cubic structure with single phase and the surface microstructural study revealed multiple grain boundaries. The Sb doping enhanced the *n*-type conduction behavior and the pentavalent Sb^{5+} was experimentally verified. Theoretical investigation using DFT revealed that the conduction band properties were mainly attributed to the Sb-5s and Sn-5s orbitals. The Sb^{5+} as the donor and the subsequent oxygen vacancy enhanced the electronic conduction. A high S value of 58.9 μV/K and $S^2\sigma$ value of 2.1 $\mu Wm^{-1}K^{-2}$ were achieved for the Sb-substituted BSO (Sb: 10 mM) at 820 K. Semiconductor to metallic transition was observed at 700 K through the charge compensation between Sb^{5+} and Sn^{4+} ions. Structural defects and grain boundary contributed to a low κ value. The dimensionless figure of merit of the Sb-substituted BSO (Sb: 10 mM) was found to be 0.28×10^{-2} at 820 K, which was larger than that of the Sb-substituted BSO (Sb: 5 mM).

Credit author statement

Palani Rajasekaran: Designed experiment, Data analysis and Manuscript writing; Yuki Kumaki: Designed and calculated theoretical band structure; Mukannan Arivanandhan: Conceptualization and investigation; M. M. S. Ibrahim Khaleeullah: Transmission electron microscopy sample preparation and image analysis; Hiroshi Nakatsugawa: Thermoelectric measurements and assistance; Ramasamy Jayavel: Validation and investigation; Yasuhiro Hayakawa: Investigation and validated the manuscript; Masaru Shimomura: Conceptualization and Supervision.

Declaration of competing interest

The authors declare that they have no known competing financial interests or personal relationships that could have appeared to influence the work reported in this paper.

Acknowledgment

The authors acknowledge the Hamamatsu Campus Center for Instrumental Analysis, Shizuoka University, for measurement facilities. The author P.R thanks JASSO scholarship and Amano Institute of Technology scholarship for the Ph. D. program.

References

[1] M. Hamid Elsheikh, D.A. Shnawah, M.F.M. Sabri, S.B.M. Said, M. Haji Hassan, M. B. Ali Bashir, M.A. Mohamad, A review on thermoelectric renewable energy: principle parameters that affect their performance, Renew. Sustain. Energy Rev. 30 (2014) 337–355, https://doi.org/10.1016/j.rser.2013.10.027.

[2] L.D. Zhao, V.P. Dravid, M.G. Kanatzidis, The panoscopic approach to high performance thermoelectrics, Energy Environ. Sci. 7 (2014) 251, https://doi.org/10.1039/c3ee43099e.

[3] H. Alam, S. Ramakrishna, A review on the enhancement of figure of merit from bulk to nano-thermoelectric materials, Nano Energy 2 (2013) 190–212, https://doi.org/10.1016/j.nanoen.2012.10.005.

[4] M.G. Kanatzidis, Nanostructured thermoelectrics: the new paradigm? Chem. Mater. 22 (2010) 648–659, https://doi.org/10.1021/cm902195j.

[5] A.D. Lalonde, Y. Pei, H. Wang, G. Jeffrey Snyder, Lead telluride alloy thermoelectrics, Mater. Today 14 (2011) 526–532, https://doi.org/10.1016/S1369-7021(11), 70278–4.

[6] N.T. Mai, D. Mott, N.T.B. Thuy, I. Osaka, S. Maenosono, Study on formation mechanism and ligand-directed architectural control of nanoparticles composed of Bi, Sb and Te: towards one-pot synthesis of ternary (Bi,Sb)2Te3, nanobuilding blocks, RSC Adv. 1 (2011) 1089–1098, https://doi.org/10.1039/c1ra00069a.

[7] S. Tongpeng, T. Sarakonsri, S. Isoda, M. Haruta, H. Kurata, C. Thanachayanont, Electron microscopy investigation of $Sb_{2-X}Bi_xTe_3$ hexagonal crystal structure growth prepared from sol-gel method, Mater. Chem. Phys. 167 (2015) 246–252, https://doi.org/10.1016/j.matchemphys.2015.10.039.

[8] R. Funahashi, I. Matsubara, S. Sodeoka, Thermoelectric properties of $Bi_2Sr_2Co_2O_x$ polycrystalline materials, Appl. Phys. Lett. 76 (2000) 2385, https://doi.org/10.1063/1.126354.

[9] Y. Wang, Y. Sui, H. Fan, X. Wang, Y. Su, W. Su, X. Liu, High temperature thermoelectric response of electron-doped $CaMnO_3$, Chem. Mater. 21 (2009) 4653–4660, https://doi.org/10.1021/cm901766y.

[10] S. Ohta, H. Ohta, K. Koumoto, Grain size dependence of thermoelectric performance of Nb-doped $SrTiO_3$ polycrystals, J. Ceram. Soc. Jpn. 114 (2006) 102–105, https://doi.org/10.2109/jcersj.114.102.

[11] Q. Liu, J. Dai, H. Li, B. Li, Y. Zhang, K. Dai, S. Chen, Optical and transport properties of Gd doped $BaSnO_3$ epitaxial films, J. Alloys Compd. 647 (2015) 959–964, https://doi.org/10.1016/j.jallcom.2015.06.014.

[12] A. Slassi, Ab initio study of a cubic perovskite: structural, electronic, optical and electrical properties of native, lanthanum- and antimony-doped barium tin oxide, Mater. Sci. Semicond. Process. 32 (2015) 100–106, https://doi.org/10.1016/j.mssp.2014.12.031.

[13] C. Huang, X. Wang, Q. Shi, X. Liu, Y. Zhang, F. Huang, T. Zhang, A facile peroxo-precursor synthesis method and structure evolution of large specific surface area mesoporous $BaSnO_3$, Inorg. Chem. 54 (2015) 4002–4010, https://doi.org/10.1021/acs.inorgchem.5b00269.

[14] R.H. Wei, X.W. Tang, Z.Z. Hui, X. Luo, J.M. Dai, J. Yang, W.H. Song, L. Chen, X. G. Zhu, X.B. Zhu, et al., Solution processing of transparent conducting epitaxial La: $BaSnO_3$ films with improved electrical mobility, Appl. Phys. Lett. 106 (2015) 1–6, https://doi.org/10.1063/1.4914972.

[15] C. Udawatte, Preparation of pure perovskite-type $BaSnO_3$ powders by the polymerized complex method at reduced temperature, Solid State Ionics 108 (1998) 23–30, https://doi.org/10.1016/s0167-2738(98)00014-9.

[16] S.S. Shin, E.J. Yeom, W.S. Yang, S. Hur, M.G. Kim, J. Im, J. Seo, J.H. Noh, S. Il Seok, Colloidally prepared La-doped $BaSnO_3$ electrodes for efficient, photostable perovskite solar cells, Science 356 (2017) 167–171, https://doi.org/10.1126/science.aam6620.

[17] H.J. Kim, U. Kim, T.H. Kim, J. Kim, H.M. Kim, B.G. Jeon, W.J. Lee, H.S. Mun, K. T. Hong, J. Yu, et al., Physical properties of transparent perovskite oxides (Ba,La) SnO_3 with high electrical mobility at room temperature, Phys. Rev. B 86 (2012) 1–9, https://doi.org/10.1103/PhysRevB.86.165205.

[18] R. Cava, P. Gammel, B. Batlogg, J. Krajewski, W. Peck Jr., L. Rupp Jr., R. Felder, R. Van Dover, Nonsuperconducting $BaSn_{1-x}Sb_xO_3$: the 5s-orbital analog of $BaPb_{1-x}B_xO_3$,, Phys. Rev. B 42 (1990) 4815–4818, https://doi.org/10.1103/PhysRevB.42.4815.

[19] H. Mizoguchi, P. Chen, P. Boolchand, V. Ksenofontov, C. Felser, P.W. Barnes, P. M. Woodward, Electrical and optical properties of Sb-doped $BaSnO_3$, Chem. Mater. 25 (2013) 3858–3866, https://doi.org/10.1021/cm4019309.

[20] M. Yasukawa, T. Kono, K. Ueda, H. Yanagi, S. Wng Kim, H. Hosono, Thermoelectric properties and figure of merit of perovskite-type $Ba_{1-x}La_xSnO_3$ with X=0.002–0.008, Solid State Commun. 172 (2013) 49–53, https://doi.org/10.1016/j.ssc.2013.08.018.

[21] R. Bourne, R. Bourne, ImageJ, Fundam. Digit. Imaging Med. 9 (2010) 185–188, https://doi.org/10.1007/978-1-84882-087-6_9.

[22] M.D. Abràmoff, P.J. Magalhães, S.J. Ram, Image processing with ImageJ, Biophot. Int. 11 (2004) 36–42, https://doi.org/10.1201/9781420005615.ax4.

[23] H. Nakatsugawa, M. Saito, Y. Okamoto, High-temperature thermoelectric properties of perovskite-type $Pr_{0.9}Sr_{0.1}Mn_{1-x}Fe_xO_3$ ($0 \leq x \leq 1$), J. Electron. Mater. 46 (2017) 3262–3272, https://doi.org/10.1007/s11664-017-5366-3.

[24] P. Giannozzi, S. Baroni, N. Bonini, M. Calandra, R. Car, C. Cavazzoni, D. Ceresoli, G.L. Chiarotti, M. Cococcioni, I. Dabo, et al., Quantum ESPRESSO: a modular and open-source software project for quantum simulations of materials, J. Phys. Condens. Matter 21 (2009), 395502, https://doi.org/10.1088/0953-8984/21/39/395502.

[25] J.P. Perdew, K. Burke, M. Ernzerhof, Generalized gradient approximation made simple, Phys. Rev. Lett. 77 (18) (1996) 3865–3868, https://doi.org/10.1103/PhysRevLett.77.3865.

[26] J.D. Pack, H.J. Monkhorst, Special points for Brillonin-zone integrations, Phys. Rev. B 16 (1977) 1748–1749, https://doi.org/10.1103/PhysRevB.16.1748.

[27] M. Eibschutz, R.J. Cava, J.J. Krajewski, W.F. Peck, W.M. Reiff, Electronic structure of $BaSn_{1-X}Sb_xO_3$, for $0.0 \leq x \leq 0.2$, Appl. Phys. Lett. 60 (1992) 830–832, https://doi.org/10.1063/1.106528.

[28] T. Maekawa, K. Kurosaki, S. Yamanaka, Thermal and mechanical properties of polycrystalline $BaSnO_3$, J. Alloys Compd. 416 (2006) 214–217, https://doi.org/10.1016/j.jallcom.2005.08.032.

[29] B.C. Luo, J. Zhang, J. Wang, P.X. Ran, Structural, electrical and optical properties of lanthanum-doped barium stannate, Ceram. Int. 41 (2015) 2668–2672, https://doi.org/10.1016/j.ceramint.2014.10.080.

[30] M. Setviń, U. Aschauer, P. Scheiber, Y.F. Li, W. Hou, M. Schmid, A. Selloni, U. Diebold, Reaction of O_2 with subsurface oxygen vacancies on TiO_2 anatase

(101), Science (80-.) 341 (2013) 988–991, https://doi.org/10.1126/science.1239879.

[31] R. Wei, X. Tang, L. Hu, X. Luo, J. Yang, W. Song, J. Dai, X. Zhu, Y. Sun, Growth, microstructures, and optoelectronic properties of epitaxial $BaSn_{1-x}Sb_xO_{3-\delta}$ thin films by chemical solution deposition, ACS Appl. Energy Mater. 1 (2018) 1585–1593, https://doi.org/10.1021/acsaem.8b00003.

[32] S.D. Ponja, B.A.D. Williamson, S. Sathasivam, D.O. Scanlon, I.P. Parkin, C. J. Carmalt, Enhanced electrical properties of antimony doped tin oxide thin films deposited: via aerosol assisted chemical vapour deposition, J. Mater. Chem. C 6 (2018) 7257–7266, https://doi.org/10.1039/c8tc01929k.

[33] S. Yanagiya, N.V. Nong, M. Sonne, N. Pryds, Thermoelectric properties of SnO_2-based ceramics doped with Nd, Hf or Bi, AIP Conf. Proc. 1449 (2012) 327–330, https://doi.org/10.1063/1.4731563.

[34] K. Rubenis, S. Populoh, P. Thiel, S. Yoon, U. Müller, J. Locs, Thermoelectric properties of dense Sb-doped SnO_2 ceramics, J. Alloys Compd. 692 (2017) 515–521, https://doi.org/10.1016/j.jallcom.2016.09.062.

[35] S.A. Miller, P. Gorai, U. Aydemir, T.O. Mason, V. Stevanović, E.S. Toberer, G. Jeffrey Snyder, SnO as a potential oxide thermoelectric candidate, J. Mater. Chem. C 5 (2017) 8854–8861, https://doi.org/10.1039/c7tc01623a.